21apZG-11 東大逆コンプトン散乱単色X線源におけるX-band電子ライナック電子ビーム試験

東大院工原子力　高エネ研[A]　石川島播磨重工[B]
坂本文人　上坂充　土橋克広　孟徳　山本智彦　夏井拓也　浦川順治[A]肥後寿泰[A]　明本光生[A]　栄久晴[B]酒井康雄[B]　金子七三雄[B]
石田大典[B]　野瀬裕之[B]

Beam experiment of X-band linac and compact Compton scattering X-ray source at the University of Tokyo

UTNS　KEK[A] IHI[B]
F. Sakamoto, M. Uesaka, T. Yamamoto, T. Natsui, J. Urakawa[A], T. Higo[A], M. Akemoto[A], H. Sakae[B], Y. Sakai[B], N. Kaneko[B], D. Ishida[B] and H. Nose[B]

東大原子力専攻では、図1に示すX-band電子線形加速器を用いた小型逆コンプトン散乱X線源の開発を進めている。このシステムは、X-band 50 MWクライストロン、X-band熱カソードRF電子銃、エネルギー選別・バンチ圧縮用アルファ電磁石、X-band進行波型加速管、Nd:YAGレーザー、X線検出器で構成されている。

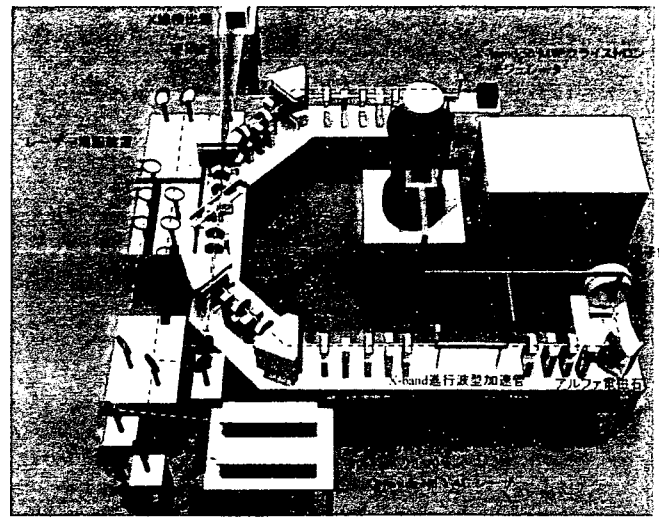

図1. 逆コンプトン散乱X線源概念図

これまでに、X-band クライストロンの大電力試験、3.5-cell X-band熱陰極RF電子銃の高電界試験、及びX-band加速管を含む立体回路とビームラインの構築を行い、高電界試験及びビーム加速試験を実施、最大40 MWの大電力を加速管に投入を達成し、約22MeVの電子ビーム加速を実証し、コンプトン散乱によるX線発生試験を実施している。本発表では、全体システムとビーム加速試験及びX線発生試験の詳細について報告する。

本システム開発は文部科学省先進小型加速器の要素技術の普及事業（平成13-17年度取りまとめ放医研）によって行われた。また、レーザーシステムとX線発生・検出システムは独立行政法人科学技術振興機構の革新技術開発研究事業の委託研究として実施されたものである。

BEAM ACCELERATION EXPERIMENT OF X-BAND LINAC FOR INVERSE COMPTON SCATTERING QUASI-MONOCHROMATIC X-RAY SOURCE AT THE UNIVERSITY OF TOKYO

Fumito Sakamoto[1,A)], Mitsuru Uesaka[A)], Tomohiko Yamamoto[A)], Takuya Natsui[A)], Yoshihiro Taniguchi[A)], Junji Urakawa[B)], Toshiyasu Higo[B)], Mitsuo Akemoto[B)], Hisaharu Sakae[C)], Masashi Yamamoto[D)]

[A)] Nuclear Professional School, the University of Tokyo
2-22 Shirakata-Shirane, Tokai, Naka, Ibaraki 319-1188, Japan

[B)] High Energy Accelerator Research Organization
1-1 Oho, Tsukuba, Ibaraki 305-0801, Japan

[C)] Ishikawajima-harima Heavy Industry
1 Shin-Nakahara, Isogo, Yokohama, Kanagawa 235-8501, Japan

[D)] Akita National College of Technology
1-1 Iijima-Bunkyo, Akita, Akita 011-8511, Japan

Abstract

We are currently developing a compact X-ray source based on laser-electron Compton scattering. To realize a compact system, we adopt an X-band linear accelerator (linac) and commercial Q-switch laser. The X-ray yield by the collision between the electron beam of 30 MeV and the Q-switch Nd: YAG laser of 1.4 J/10 ns (second harmonic) is 10^7 photons/RF pulse (10^8 photons/s for 10 pps). The injector of this system consists of an X-band thermionic cathode RF gun and an alpha magnet. So far, we have constructed the whole RF system and beam line for the X-band linac and achieved 2 MeV electron beam generation from the X-band thermionic cathode RF gun. In addition, we achieved 40 MW RF feeding to the accelerating structure and beam the beam energy of 22 MeV were observed just after the accelerating structure. The laser system for the X-ray generation via Compton scattering was also constructed and evaluated its properties. In this paper, we will present the details of our system and progress of beam acceleration experiment and the performance of the laser system for the Compton scattering experiment. This work is performed under the national project of Development of Advanced Compact Accelerators in Japan and is partially supported by the Research Program on Development Innovative Technology (#0494) of the Japan Science and Technology Agency and in part supported by Health and Labour Sciences Research Grants.

東大逆コンプトン散乱準単色X線源 におけるX-band電子ライナックビーム加速試験

1．はじめに

単色X線は医療、生命科学、材料科学など広い分野で利用されている。単色X線は、既存X線応用技術の高精度/高度化だけでなく、新しい技術への期待もある。2色X線CT[1]がその例であり、これはエネルギーの違う2種類の単色X線を用いて、物質のエフェクティブな元素番号の分布を得ようとするものであり、単色X線は必要不可欠である。単色X線源として第3世代放射光施設に代表される放射光施設が用いられているが、高額巨大な装置であり、普及性には難がある。GeV程度のエネルギーの電子貯蔵リングで生成できるX線に相当するようなエネルギーのX線を生成可能な超小型のX線源を実現するための方策として、大強度のレーザー光と電子ビームを衝突させてコンプトン散乱により高エネルギーX線を得る方法がある[2-5]。我々は、X-band (11.424 GHz) ライナックを用いたより小型のX線源の開発を進めている[6,7]。

東京大学大学院工学系研究科原子力専攻にて進めているシステム概念図を図1に示す。これまでに、X-bandクライストロン（Toshiba E3768）の大電力試験と、3.5-cell X-band 熱陰極高周波 (RF) 電子銃の高電界試験及びビーム生成試験を行ってきており、2 MeV の電子ビーム発生を確認している[5]。電子銃からの電子発生に引き続き、ビーム加速に用いるX-band加速管とビーム輸送用ビームラインの据付を終え、全RFシステムへの大電力投入試験を実施し、最大で40　MW (加速管30 MW, 電子銃4 MW @ 150 ns) の大電力投入を達成した。熱陰極RF電子銃からの電

[1] E-mail: saka@nuclear.jp

子ビームを加速管へ入射し、最大22 MeVの電子ビーム加速を達成した。同時に、コンプトン散乱実験に用いるNd: YAGレーザーの光学系の構築も完了し、電子ビーム衝突点において十分な安定度を有している事を確認した。現在はコンプトン散乱によるX線発生試験を実施している。

本発表では、X-bandライナックによるビーム加速試験の詳細と、コンプトン散乱によるX線発生試験について報告する。

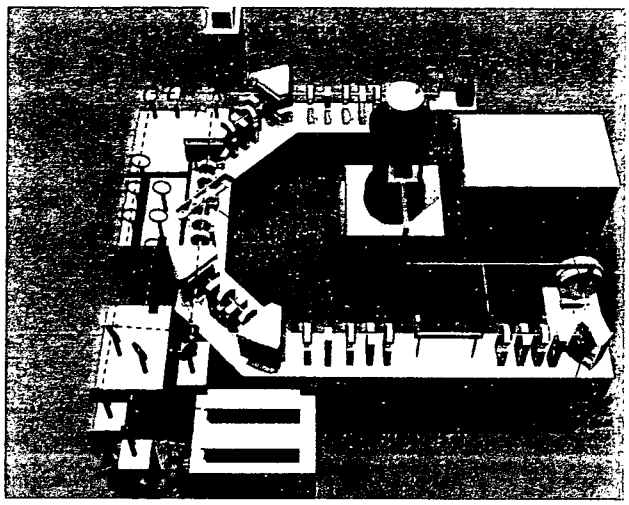

図1　東大逆コンプトン散乱X線源概念図

2. X-bandライナック高電界試験とビーム加速試験

図2にX-band熱陰極RF電子銃とX-band進行波型加速管を含む全RF立体回路システムを示す。クライストロン出力を7 dB方向性結合器により4:1の割合で分割し、クライストロン出力50 MW時40 MWを加速管へ、6 MWをRF電子銃へフィードする設計となっている。加速管は空洞内での電場分布を考慮するため、軸対象なダブルフィードタイプとなっている。加速管入力カプラ手前の3 dB方向性結合器によりRFを分割している。この方向性結合器における位相差は、ネットワークアナライザーにより測定・調整し、1度以内に合わせ込んでいる。全RFシステムのRFコンディショニング履歴を図3に示す。これまでに、10 Hz運転においてクライストロン出力約40 MW 120 nsを達成している。図4及び図5に各方向性結合機において検波器により観測されたRF波形を示す。図5のCh:3及びCh.4はそれぞれアルファ電磁石前後においてCTにより測定されたビーム電流を示しているが、電子銃よりピーク電流約100 mAの電子ビームが得られているのがわかる。この電子ビームを加速管入り口へと輸送し、ビーム加速を実施した結果、加速管後の偏向電磁石によるエネルギー測定により、22 MeVの電子加速を確認した。しかしながら、加速管後のスクリーンモニター（アルミナセラミックス）によってビームプロファイルは観測されるものの、加速管以後でのビームロスが非常に大きく、電流値が極めて低いため、今後ビーム輸送の最適化を実施する必要がある。電子ビームのエミッタンス、バンチ長等の特性評価は、今後計画している。ビーム加速の成功に引き続き、電子ビームをレーザーパルスとの衝突点へ輸送し、コンプトン散乱によるX線発生試験体系の構築を行った。

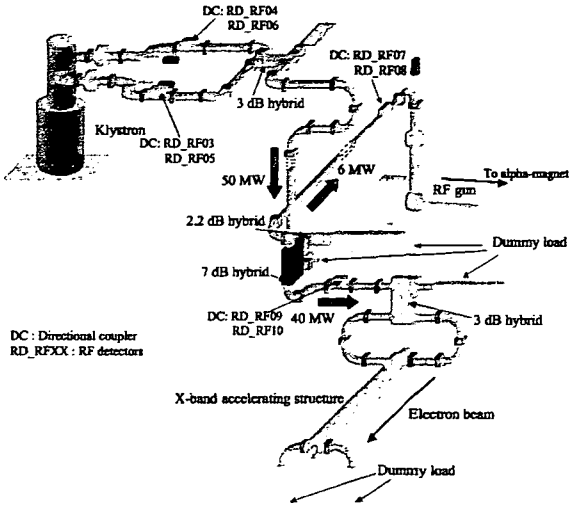

図2　X-bandライナックRF立体回路模式図

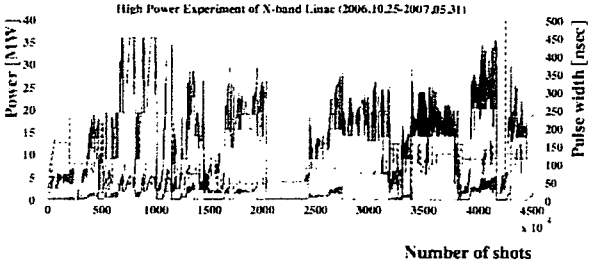

図3 X-bandライナックRFプロセッシング履歴例

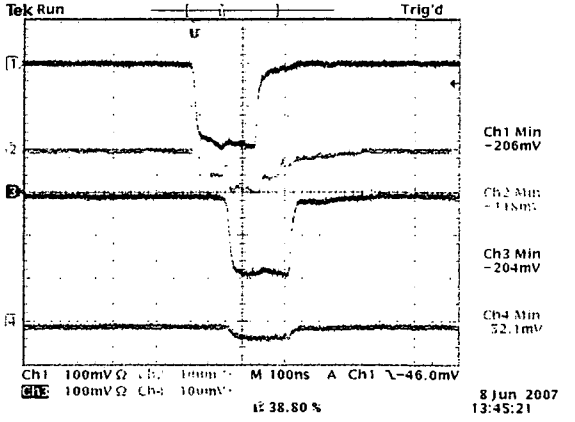

図4 典型的なRF波形(Ch.1:クライストロン出力電力、Ch.2:クライストロンへの反射電力、Ch.3:加速管への入力電力、Ch.4:加速管からの反射電力)

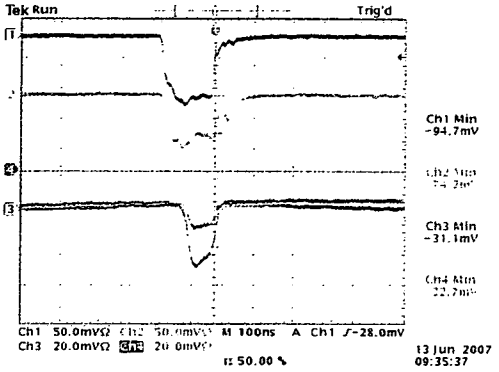

図5 典型的なRF波形(Ch.1:RF電子銃への入力電力、Ch.2:RF電子銃からの反射電力、Ch.3:アルファ電磁石前でのビーム電流、Ch.4:アルファ電磁石後でのビーム電流)

3. コンプトン散乱単色X線生成実験

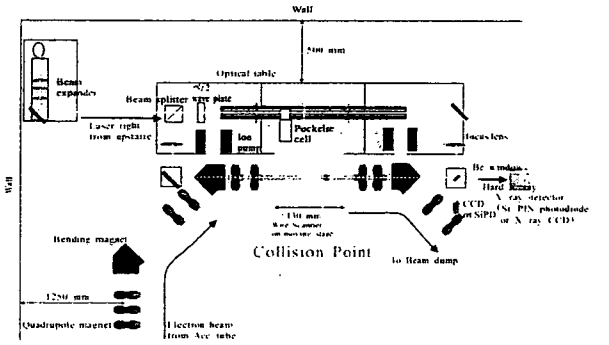

図6 コンプトン散乱X線発生実験体系

図6にコンプトン散乱X線生成のための実験体系概念図を示す。レーザー装置は地上に設置されており、ミラーによりピット内に輸送される。レーザー光は下流側偏向電磁石からビームラインに入射され、電子ビームとの衝突後、上流側偏向電磁石で大気中に取り出され、周回路に入る。コンプトン散乱により生成されたX線は、下流側偏向電磁石で電子ビームと分離され、その先の厚さ3 mmのレーザー用ミラーと厚さ100 μmのBe窓を貫いて大気中に取り出され、X線検出器に入射する。X線検出器には、NaIシンチレータ及びSi photo-diodeの使用を検討している。衝突点に設置してあるビーム診断用チェンバーは、Wire Scanner、蛍光板、ナイフエッジが一体化した構造になっており、電子ビーム・レーザー両方のプロファイルと位置を計測できるようになっている。また、このチェンバーはビーム軸方向に±130 mmの可動ステージに設置しているため、衝突点前後におけるビーム軌道や、正確なwaistの位置が計測可能なシステムになっている。電子・レーザー衝突試験に先立ち、レーザーシステムの性能評価試験を実施した。図8に衝突点でのレーザースポットサイズの時間変動を示すが、ビームサイズ、位置、強度共に、10 %以下の安定度を有している事が確認されている。

現在、加速管後の電子ビームを衝突点まで輸送し、電子・レーザー衝突によるX線生成試験を繰り返し実施している。図9に衝突点における電子・レーザー双方のビームプロファイルを示す。

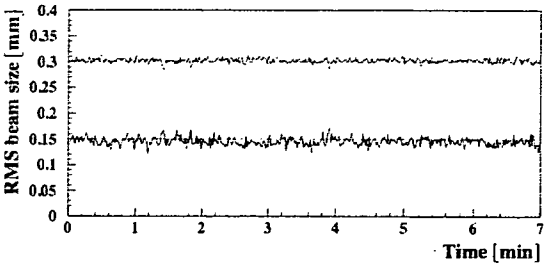

図8 電子ビーム・レーザー衝突点におけるレーザースポットサイズの安定性（赤:hirizontal、青:vertical)

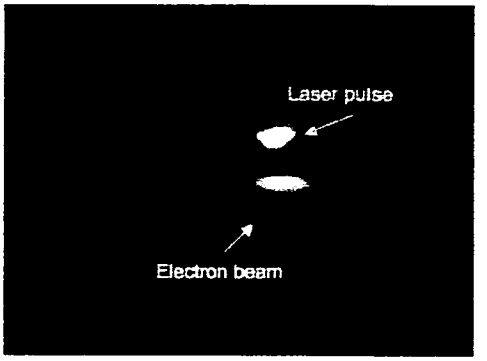

図9 電子ビーム・レーザー衝突点における電子ビーム、レーザービームプロファイル

4. まとめと今後の予定

東大原子力専攻においてX-band電子ライナックを用いたコンプトン散乱単色X線源を開発である。これまでにX-band熱陰極RF電子銃によるビーム生成を達成し、X-band加速管を含む全RF立体回路システムの構築を行った。高電界試験を実施し、クライストロンの電力投入を達成した。RF電子銃により生成したマルチバンチ電子ビームを加速管へ輸送し、22 MeVの電子加速を達成した。現在は電子・レーザー衝突点へビーム輸送を達成しており、コンプトン散乱によるX線生成試験を実施している。今後、電子ビーム特性評価及びX線特性評価を順次実施していく予定である。

参考文献

[1] M. Torikoshi et. al., , *J. Biomedical Opt.* **6**, 371 (2001)
[2] R. Kuroda et. al., *Proc. of the European Particle Accelerator Conference*, Edinburgh, Scotland, (2006)
[3] F. Carroll, *Am. J. Rentgenol.* **181**. 1197 (2003)
[4] W. J. Brown, et. al., *Phys. Rev. ST.* 7, 060702 (2004)
[5] E. Vlieks, et. al., *Proc. of the European Particle Accelerator Conference*, Lucerne, Switzerland, (2004)
[6]F. Sakamoto, et. al., *J. Korean Phys. Soc.*, 49,1 (2006) 286.
[7]K. Dobashi, et. al., *Jpn. J. Appl. Phys.*, 44 (2005) 1999

Available online at www.sciencedirect.com
ScienceDirect
ELSEVIER
Nuclear Instruments and Methods in Physics Research B 261 (2007) 867–870
NIM B
Beam Interactions with Materials & Atoms
www.elsevier.com/locate/nimb

Monochromatic tunable Compton scattering X-ray source using X-band multi-bunch linac and YAG laser circulation system

Mitsuru Uesaka [a,*], Fumito Sakamoto [a], Katsuhiro Dobashi [a], Tatsuo Kaneyasu [b], Tomohiko Yamamoto [a], De Meng [a], Junji Urakawa [c], Toshiyasu Higo [c], Mitsuo Akemoto [c], Hitoshi Hayano [c]

[a] *Nuclear Professional School, University of Tokyo, 2-22 Shirakata-Shirane, Tokai, Naka, Ibaraki 319-1188, Japan*
[b] *Institute for Molecular Science, Myodaiji, Okazaki, Aichi, Japan*
[c] *High Energy Accelerator Development Organization, 1-1, Oho, Tsukuba Ibaraki, Japan*

Available online 1 May 2007

Abstract

We are currently developing a compact monochromatic X-ray source based on laser–electron collision. To realize remarkably compact, high-intensity and highly-stable-system, we adopt an X-band multi-bunch liner accelerator (linac) (30 MeV 10^4 micro-bunches of 20 pC for 1 μs RF pulse at 12.5 Hz) and commercial Q-switch laser. The X-ray yields by the multi-bunch electron beam and Q-switch Nd:YAG laser of 2.5, 1.4 J/10 ns (FWHM) (1064, 532 nm (second harmonic)) are 1×10^9, 0.5×10^9 photons/s, respectively. So far we have achieved beam generation from the X-band thermionic cathode RF gun. The beam energy is 2 MeV. This experimental high energy (~2 MeV) beam generation from the X-band thermionic cathode RF gun is the first achievement in the world. In this paper, we describe the details of our X-band linac system, experimental results of X-band thermionic cathode RF gun and present status of the whole system of the Compton scattering X-ray source. Numerical CT (computed tomography) simulation for the application of the monochromatic X-rays is also reported.

PACS: 29.27.Eg; 29.17.+W; 52.59.Px

Keywords: X-band electron linear accelerator; Q-switch YAG laser; Multi-collision Compton scattering scheme; Laser circulation system; Dual-energy X-ray CT

1. Introduction

X-rays of 10–40 keV are of great use in several research fields. Example techniques that use such monochromatic X-rays are dual-energy X-ray CT [1] and subtraction imaging using a contrast agent and dual energy X-rays.

Intense high energy (10–40 keV) X-rays are generated by the synchrotron radiation (SR) light source. However, most SR sources are too large to be widely used for monochromatic X-rays. One solution to realize a remarkable compactness is laser–electron collision. Recently, many facilities are developing a Compton scattering X-ray source that consists of an electron linac and laser system [2,3]. However, most of them adopt the scattering between an ultra-short single electron bunch and an ultra-short single laser pulse to obtain ultra-short pulse X-ray beam. Therefore, they suffer the fluctuation of the X-ray intensity due to the timing jitter between the electron bunch and the laser pulse. In order to overcome this weak point of Compton scattering X-ray source, one solution would be multiple scattering between multi-bunch electron beam and long-pulse laser beam. At the University of Tokyo, we are developing a more compact, high-intensity and high-stable Compton scattering X-ray source. Our system consists of an X-band (11.424 GHz) multi-bunch electron linac and

* Corresponding author. Tel.: +81 29 287 8421;fax: +81 29 287 8488.
E-mail address: uesaka@nuclear.jp (M. Uesaka).

0168-583X/$ - see front matter © 2007 Elsevier B.V. All rights reserved.
doi:10.1016/j.nimb.2007.04.269

a Q-switch Nd:YAG laser. To demonstrate the proposed X-ray source, an X-band linac beam line for a proof-of-principle experiment is under construction [4,5]. So far, we have achieved 2 MeV electron beam generation from the RF gun [6]. In this paper, we will report the details of the beam generation experiment of the 3.5-cell X-band thermionic cathode RF gun and present status of whole system of the Compton scattering X-ray source. Details of the numerical CT simulation for application of the monochromatic X-rays are also reported in this paper.

2. Monochromatic tunable Compton scattering X-ray source

Fig. 1 shows schematic and photograph of the compact X-ray source at the University of Tokyo. Multi-bunch electron beam (30 MeV 10^4 micro-bunches of 20 pC for 1 μs RF pulse at 12.5 Hz) generated by a 3.5-cell X-band thermionic cathode RF gun is collimated and compressed by an alpha magnet and accelerated by a 0.5 m X-band traveling type accelerating structure. The alpha magnet generates graded dipole field to form the alpha-shaped electron trajectory and plays a role of energy filter to cut electrons of large emittance by horizontal slits. The electron beam is bent by achromatic bends and focused at the collision point. The thermionic cathode RF gun can generate a high-current (2 μA) multi-bunch (10^4 bunches in 1 μs) electron beam. A 0.5 m X-band accelerating structure is used for the X-ray source. In order to concentrate on the R&D of the accelerator, we chose a Q-switched Nd:YAG lasers with an intensity of 2.5, 1.4 J/pulse, a repetition rate of 10 pps, a pulse duration of 10 ns (FWHM) and a wavelength of 1064, 532 nm (second harmonic), respectively. The X-band thermionic RF gun realizes 10^4 multi-bunches of 20 pC per micro-bunch. Moreover, we adopt a laser pulse circulation system to increase the time-integrated colliding laser energy by about 10 times. We already confirmed the circulation experimentally. Finally, the multiple collision between the multi-bunches and circulated laser pulse gives the X-ray yield of 10^9 photons/s. The X-ray yields by the multi-bunch electron beam and Q-switch Nd:YAG laser of 2.5, 1.4 J/10 ns (FWHM) (1064, 532 nm (second harmonic)) are 1×10^9, 0.5×10^9 photons/s, respectively.

3. X-band thermionic RF gun and current status of the whole system of the X-ray source

So far, we have performed a high-power and beam generation experiment of the X-band thermionic cathode RF gun [6]. Cut-view and photograph are shown in Fig. 2. Fig. 1(b) shows a photograph around the 0.5 m X-band accelerating structure. The energy spectrum of the electron beam is estimated by using the inner slit of the alpha magnet to observe the transmission of the beam current. Fig. 3 shows the energy spectrum of the electron beam measured by using the alpha magnet. The peak energy is 2 MeV. The nominal beam current and the charge per bunch are 2 μA and 20 pC/bunch, respectively. However, the measured parameters are not consistent with the design values. The reason of the lower established mean energy was found to be the trouble of the stainless spring between the cathode rod and cavity tube. We thought that the stainless spring played both roles of RF shielding and high thermal impedance. Although we operated the thermionic cathode below the melting point of stainless, the spring was partially evaporated and sputtered to the inner surface of the gun cavity. Then, the Q-value and field gradient was degraded. We analyses this effect by SUPERFISH code (cavity design) and PARMELA code (beam transport) and met the agreement with the measured electron energy. We already replaced the stainless spring to W-spring to avoid this problem.

For the next step, we are constructing a beam line of the X-band accelerating structure and Nd:YAG laser system for Compton scattering experiment. The multi-bunch electron beam is accelerated up to 30 MeV, and is bent by achromatic bends and focused at the collision point. We will start the high-power RF feed and beam acceleration test of the X-band accelerating structure soon and Compton scattering experiment is planed.

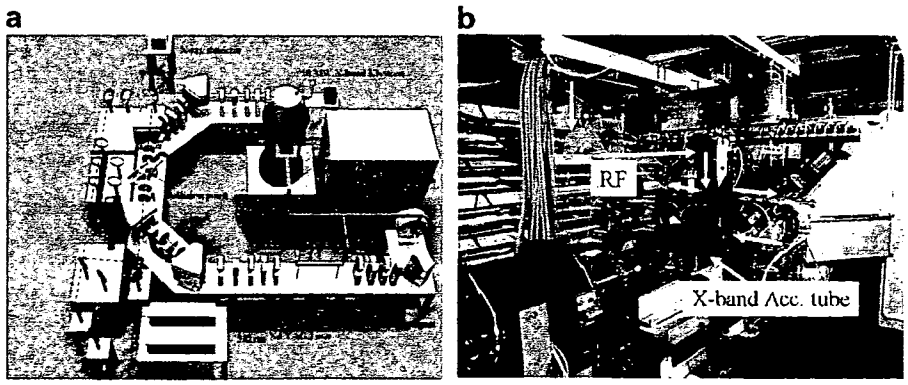

Fig. 1. Laser–electron Compton scattering monochromatic tunable X-ray source (schematic bird-eye view (a) and updated photograph around the accelerating structure (b)).

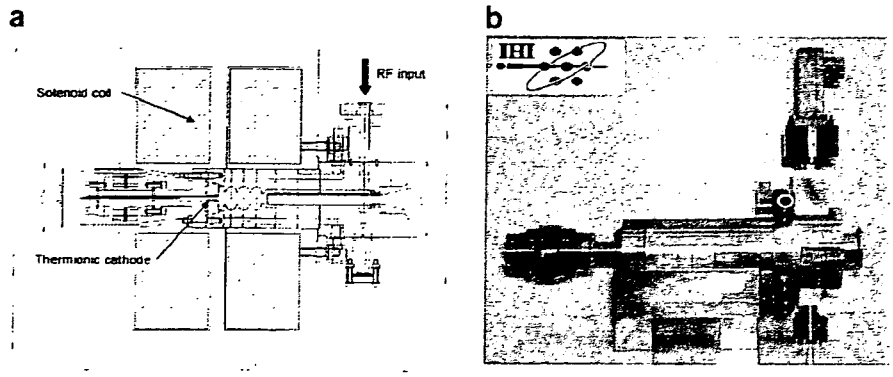

Fig. 2. 3.5-cell X-band thermionic cathode RF gun cavity: cross section (a) and photograph (b).

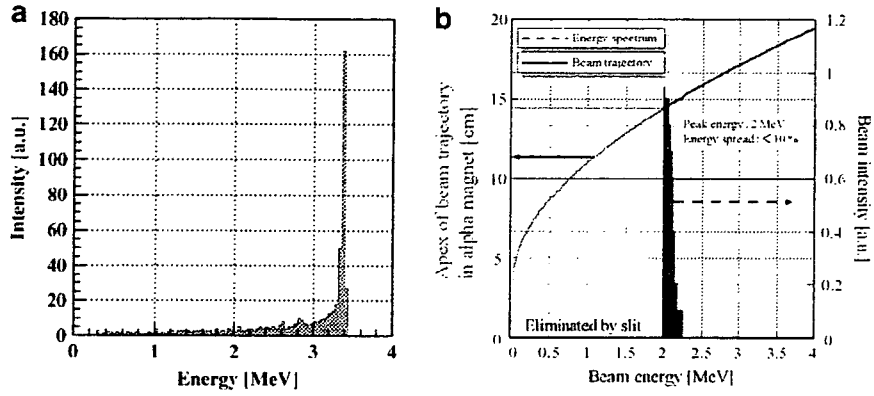

Fig. 3. Designed (a) and measured (b) energy spectra of the electron beam emitted by the gun.

4. Application to dual-energy X-ray CT for medical use

Effective atomic number Z_{eff} and electron density ρ_e are obtained by linear attenuation coefficients of a material using two monochromatic X-rays with different energies. A linear attenuation coefficient μ of a material is approximately written as a function of atomic number Z and X-ray energy E using a formula proposed by Jackson and Hawkes [7] as follows:

$$\mu(Z,E) \simeq \rho\frac{N_A}{A}Z\left\{4\sqrt{2}Z^4\alpha^4\left(\frac{mc^2}{E}\right)\phi_0\sum_{nu'}f_nu' + \sigma_{KN} + \frac{Z(1-z^{b-1})}{Z'^2}\sigma_{SC}^{coh}(Z',E')\right\} = \rho_e(Z^4F(Z,E)+G(Z,E)), \quad (1)$$

where ρ is mass density, N_A is Avogadro's number, A is atomic mass, f_nu' is the collection terms for photoelectric absorption cross section, σ_{KN} is the Klein–Nishina cross section and σ_{SC}^{coh} is the coherent scattering cross section of the standard element Z' at energy of $E' = (Z'/Z)^{1/3}E$.

In the equation, parameter b is proposed to be 0.5 and the standard element is oxygen [7]. When linear attenuation coefficients are measured for two energies E_1 and E_2, one can extract effective atomic number Z_{eff} and electron density ρ_e solving following equations:

$$Z^4 = \frac{\mu(E_2)G(Z,E_1) - \mu(E_1)G(Z,E_2)}{\mu(E_1)G(Z,E_2) - \mu(E_2)G(Z,E_1)}, \quad (2)$$

$$\rho_e = \frac{\mu(E_1)F(Z,E_2) - \mu(E_2)F(Z,E_1)}{F(Z,E_2)G(Z,E_1) - F(Z,E_1)G(Z,E_2)}. \quad (3)$$

The effective atomic number Z_{eff} is defined for a compound or a mixture as:

$$Z_{\text{eff}} = \left(\sum_i q_i Z_i^k\right)^{1/k}, \quad (4)$$

where q_i is the fractional electron content of ith element in the compound or the mixture and the parameter $k = 4$.

Numerical CT simulation has been carried out with low to medium Z elements. Though the energy spread of monochromatic X-ray is 1–10%, the X-ray energy profile depends on the scattering angle. Therefore, the energy spread of X-ray in a pixel is in the order of 0.1%. The small energy spread in a pixel is an advantage of the Compton scattering X-ray source for the dual-energy X-ray CT. We assumed CT system shown in Fig. 4(a) with cylindrical samples. The diameter of the sample is 20 mm and the pixel size of the detector is 0.1 mm. First, light elements of

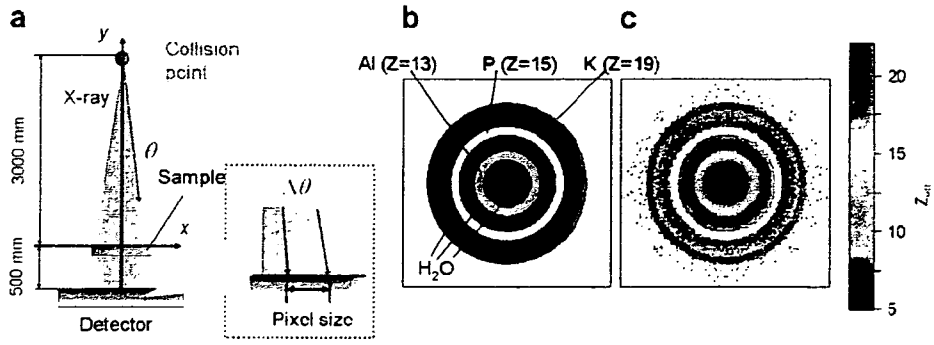

Fig. 4. Schematic drawing of the dual-energy X-ray CT system using the compact monochromatic hard X-ray source (a), input atomic number distribution in the sample (b) and reconstructed atomic number distribution (c).

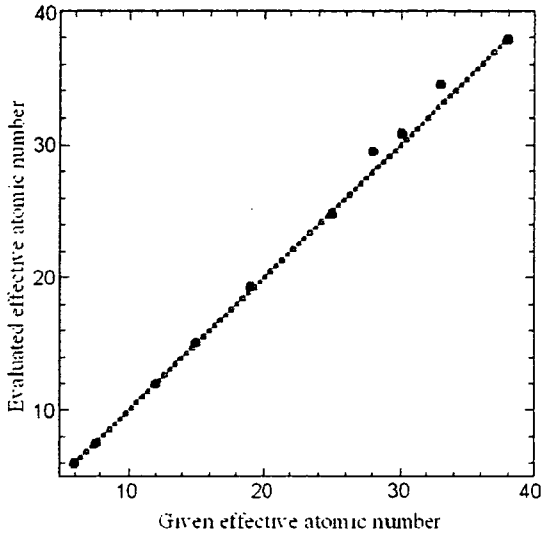

Fig. 5. Comparison of given effective atomic number and evaluated ones. The maximum error is about 3% (rms) for $Z = \sim 30$.

$Z = 13$, 15 and 19 with water as presented in Fig. 4(b) is tested. Reconstructed cross sectional images of the sample based on linear attenuation coefficients are obtained for two energies. Atomic number in the image is derived from linear attenuation coefficients based images. Two-dimensional images based on effective atomic number distribution in the sample and the reconstructed images are shown in Fig. 4(c). This analysis can be applied to medium Z elements up to $Z = 38$. Comparison of given effective atomic number and evaluated ones was performed as shown in Fig. 5. Maximum error is about 3% (rms) for $Z = \sim 30$. We are going to make use of a certain filter function in the CT algorithm to get smoother distribution at the next step. It could contribute to improve the evaluation resolution. We are going to use the HARP (high-gain Avalanche rushing amorphous photoconductor [8]) X-ray camera. Based on its sensitivity, we estimate to achieve 2×10^7, 10^7 photons/mm^2/s for 21.9, 43.8 keV and 10 images per second with 100 μm × 100 μm pixel and area of 20 mm diameter at 1 m distance from the X-ray emission point.

5. Conclusion

We are developing the compact, highly-intensity and highly-stable-Compton scattering X-ray source based on X-band multi-bunch electron linac and reliable Nd:YAG laser. The X-ray yields by the multi-bunch electron beam and Q-switch Nd:YAG laser of 2.5, 1.4 J/10 ns (FWHM) (1064, 532 nm (second harmonic)) are 1×10^9, 0.5×10^9 photons/s, respectively. So far, we have achieved the beam generation from the X-band thermionic cathode RF gun. The beam energy is 2 MeV. This experimental high energy (~2 MeV) beam generation from the X-band thermionic cathode RF gun is the first achievement in the world. For the next stage, we will perform the experiments on the beam acceleration and the Compton scattering X-ray generation soon.

We have examined the applicability of the dual-energy X-ray CT using the compact hard X-ray source by a numerical simulation. Low to medium Z elements up to $Z = 38$ are well identified with X-ray energies of 21.9 keV and 43.8 keV.

References

[1] M. Torikoshi et al., IEEE Trans. Nucl. Sci. 50 (2003) 5.
[2] F. Carroll, Am. J. Roentgenol. 181 (2003) 1197.
[3] W.J. Brown et al., Phys. Rev. ST 7 (2004) 060702.
[4] K. Dobashi et al., Jpn. J. Appl. Phys. 44 (2005) 1999.
[5] A. Fukasawa et al., Nucl. Instr. and Meth. B 241 (2005) 905.
[6] F. Sakamoto et al., J. Korean Phys. Soc. 49 (2006) 286.
[7] D.F. Jackson, D.J. Hawkes, Phys. Rep. 70 (1981) 169.
[8] M. Kubota et al., IEEE Trans. Broadcast. 42 (3) (1996) 251.

Available online at www.sciencedirect.com
ScienceDirect
Nuclear Instruments and Methods in Physics Research B 261 (2007) 52–55
NIM B
Beam Interactions with Materials & Atoms
www.elsevier.com/locate/nimb

High power laser pulse circulation experiment for compact quasi-monochromatic tunable X-ray source

De Meng [a,*], Fumito Sakamoto [a], Tomohiko Yamamoto [a], Katsuhiro Dobashi [a], Mitsuru Uesaka [a], Hiroyuki Nose [b], Daisuke Ishida [b], Namio Kaneko [b], Yasuo Sakai [b]

[a] *Nuclear Professional School, University of Tokyo, 2-22 Shirakata-Shirane, Tokai, Naka, Ibaraki 319-1188, Japan*
[b] *Ishikawajima-Harima Heavy Industries Co., Ltd., Toyosu Ihi Building, 1-1, Toyosu 3-chome, Koto-ku, Tokyo 135-8710, Japan*

Available online 1 May 2007

Abstract

Laser electron Compton scattering monochromatic tunable X-ray source using X-band (11.424 GHz) electron linear accelerator and Q-switch Nd:YAG laser is under construction at Nuclear Professional School, the University of Tokyo. To enhance the X-ray intensity, we installed a laser circulation system. Now, we are performing the circulation experiment by using a high power laser (1.4 J, 532 nm). We confirmed the laser pulse circulated in the optical circuit more than 15 times and the laser intensity is enhanced about 3.5 times.

PACS: 29.27.Eg; 42.15.Eq; 42.60.–v; 42.60.By

Keywords: X-band electron linear accelerator; Q-switch YAG laser; Multi-collision Compton scattering scheme; Laser circulation system

1. Introduction

Monochromatic X-rays are very useful for medical science, biology and material science, etc. For example, it is used in dynamic intravenous coronary arteriography (IVCAG), monochromatic X-ray CT, subtraction imaging and dual-energy X-ray CT. Experiments of dual-energy X-ray CT have been performed by using synchrotron radiation light sources to measure electron density in biological materials [1]. The technique of dual-energy X-ray CT can be used in various fields such as treatment planning for advanced radiotherapy in medicine and inspection of hazardous substance for homeland security. However, most SR sources are too large and too expensive to be applied and used widely for public use. Therefore, we are developing a compact monochromatic tunable X-ray source (10–40 keV) based on laser electron Compton scattering at the Nuclear Professional School, the University of Tokyo. The demonstration system of the monochromatic tunable X-ray source is shown in Fig. 1(a).

In order to realize stable X-ray generation, we adopted multi-bunch electron beam (10^4 bunches/1 μs RF pulse, 25 MeV) from an X-band (11.424 GHz) linac and 10 ns reliable Q-switch Nd:YAG laser (1.4 J, 532 nm and 2.5 J, 1064 nm) [2]. It is calculated that the X-ray yield by the electron beam (25 MeV) and a Q-switched Nd:YAG laser (2.5 J, 1064 nm) is about 10^8 photons/s. In the case of laser-electron Compton scattering, since the X-ray energy depends on electron energy and laser wavelength, by introducing two different wavelength (532 nm, 1064 nm) lasers and optical switch, we can generate dual energy X-ray, and change its energy rapidly (40 ms). Advantage of this dual energy system is that the dual energy X-ray CT or subtract X-ray CT can be adapted to the living specimens.

In order to expand the range of applications of this monochromatic tunable X-ray source, there is a need to increase the intensity of the X-ray. We adopted a method that can recycle the laser pulse and enhance the luminosity

* Corresponding author. Tel.: +81 29 287 8413; fax: +81 29 287 8488.
E-mail address: dmou@nuclear.jp (D. Meng).

0168-583X/$ - see front matter © 2007 Elsevier B.V. All rights reserved.
doi:10.1016/j.nimb.2007.04.270

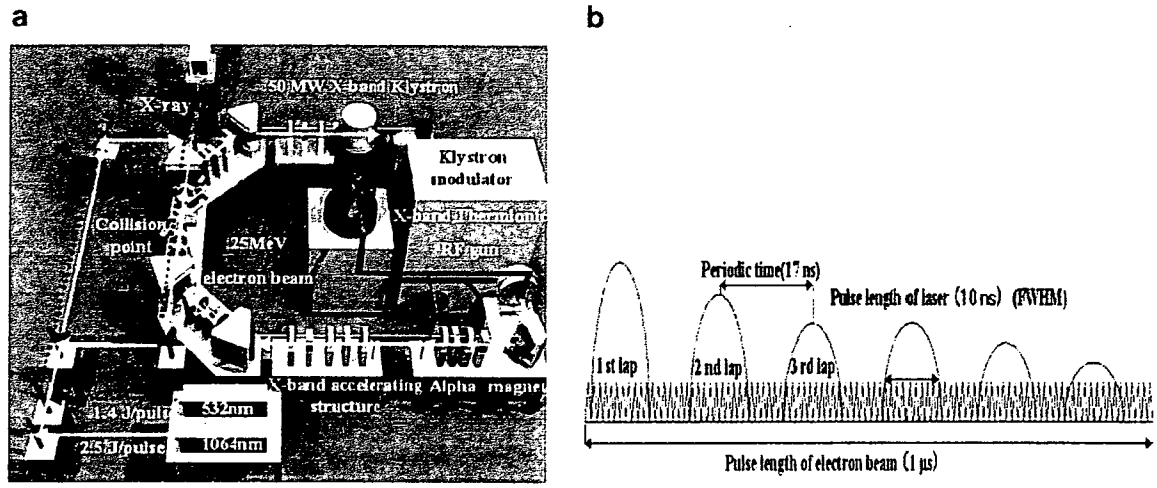

Fig. 1. Laser-electron Compton scattering monochromatic tunable X-ray source (a). We adopted a method that circulates a laser pulse and enhance the luminosity up to 10 times (b).

up to 10 times. Since the pulse length of the electron beam (1 μs) is 100 times larger than the pulse length of the laser pulse (10 ns [FWHM]), most of the electron bunches are available for multi-scattering with multiple laser pulses. In order to generate X-ray more efficiently, we have adopted a laser pulse circulation system. The purpose of this research is the construction of laser pulse circulation system for laser-electron Compton scattering. Effect of adapting laser circulation system is shown in Fig. 1(b).

2. Advantages by installing the laser pulse circulation system

Since the pulse length of the Q-switch Nd:YAG laser is 10 ns [FWHM] which is shorter than the electron beam length (1 μs), most electron bunches do not contribute to the X-ray generation. The X-ray intensity in this scheme is calculated to be 10^8 photons/s, which is low for the application. To increase the X-ray intensity, we installed a laser pulse circulation system. By adopting the laser pulse circulation system, we can let a single laser pulse repeatedly collide with multi-bunch electron beam by switching the polarization state of the laser pulse. In addition we can let the laser pulse more accurately collide with electron beam by controlling the position of laser pulse at the collision point. This means we can achieve the collision between multi-bunch electron beam and laser pulse more efficiently, and the X-ray yield increases.

2.1. Principle of laser pulse circulation in optical circuit

The schematic layout of laser pulse circulation is shown in Fig. 2(a). The optical circuit is consisted of polarization beam-splitter, half-wave plat, mirror, and pockels-cell. At first, a laser pulse is injected into the optical circuit with P-polarization. When this laser pulse passes through the half-wave plat, the polarization plane of laser pulse is rotated 90°, the P-polarization turns into S-polarization. This S-polarization laser pulse is reflected by the polarization beam-splitter and enters the optical circuit once again. After passing through the half-wave plat, the S-polariza-

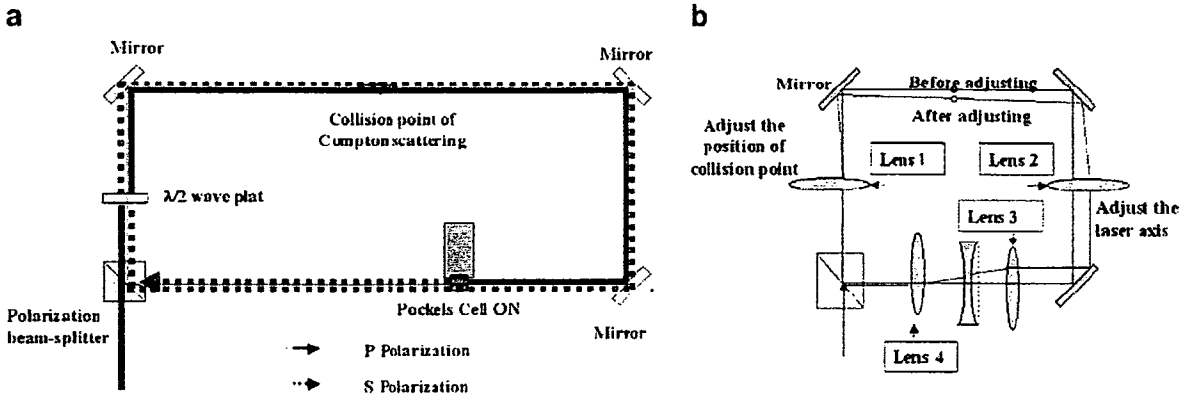

Fig. 2. Advantages by installing the laser pulse circulation system. By blocking a laser pulse into an optical circuit, the laser pulse (10 ns [FWHM]) collides with multiple electron pulse (1 ms) repeatedly (a). We let the laser pulse more accurately collide with electron beam by controlling the position of laser pulse by the four convex lenses at the collision point (b).

tion turns into P-polarization. Before the laser pulse reaches pockels-cell, we turns on the pockels-cell to rotate the polarization plane of laser pulse by 90°. Consequently after 2nd lap, the laser pulse always enters in the polarization beam-splitter with S-polarization, and the laser pulse will be locked into the optical circuit.

2.2. Upgrade of the laser pulse circulation system

Total intensity of laser pulse can be calculated using geometric series. Total laser energy I_{total} in the laser circulation system is written as

$$I_{\text{total}} = \sum_{n=1}^{N} I_0 A^{n-1} = I_0 \frac{1-A^n}{1-A} \quad (1)$$

where I_0 is the initial laser energy, A the transmission efficiency per circulation, and N the total number of circulations. For example, if the transmission efficiency per circulation $A = 0.9$ and the total number of circulations $N = 50$, we expect the laser intensity to increase by 10 times. Therefore, it is calculated that the X-ray intensity will rise up to 10^9 photons/s by installing the laser pulse circulation system.

3. Precise control of laser beam spot at collision point

In the laser-electron Compton scattering experiment, it is necessary to change the light axis of the laser beam to match the electron beam accurately at the laser-electron collision point. To adjust the light axis of the laser beam, we usually adjust the angle of mirrors. But there is a limitation of the adjusting range. To realize a precise control, we propose a method by adjusting four convex lenses to control the laser beam position at collision point. Fig. 2(b) shows the principle of adjusting the laser beam position. At first we adjust lens 1 to change the transverse position of the laser beam spot at the collision point. Then, we adjust lens 2 to correct the tangent of the laser trace. Finally, we adjust lens 3 and lens 4 to eliminate the tangent. By using this method we can control the laser beam spot more effectively than controlling the angle of mirrors.

4. Experiment

We had carried out proof-of-principle experiments with low power fundamental laser and harmonic laser (25 mJ 532 nm, and 50 mJ, 1064 nm) [3,4]. On the basis of the proof-of-principle experiment, now we are carrying out laser circulation experiment with the high power YAG laser of 2nd harmonic (1.4 J, 532 nm). Experimental setup of high power laser pulse circulation system is illustrated in Fig. 3.

After the beam size and tangent are adjusted by a beam expander and beam steerer, the laser pulse is injected into the optical circuit with P-polarization. Then, the laser pulse will be locked into the optical circuit [5]. At the collision point, the laser pulse (10 ns [FWHM]) collides with electron multi-bunches (1 μs) repeatedly. Updated photograph of the laser pulse circulation system is shown in Fig. 3(a). We measure the laser position and beam size at collision point by the beam profiler, and measure the laser intensity by the photo-multiplier. In order to check the repeatability of the proof-of-principle experiments, we reduce the laser intensity by 1/2800 (0.5 mJ).

5. Results

Fig. 4 shows the laser intensity measured by the photo-multiplier. The signal indicates that the laser pulse is locked into the optical circuit more than 15 times. Since the laser intensity of 1st lap is 1.6 and that of 9th lap is 0.2, then we obtained $A = 0.71$ and $I_{\text{total}}/I_0 = 3.5$. Therefore, we confirmed that the laser intensity is enhanced about 3.5 times. However, according to the waveform of laser intensity, there is a strong attenuation between the intensity of 1st lap and 2nd lap. Additionally the attenuation at odd laps and even laps are different. We think these phenomena are caused by different laser paths at odd and even laps.

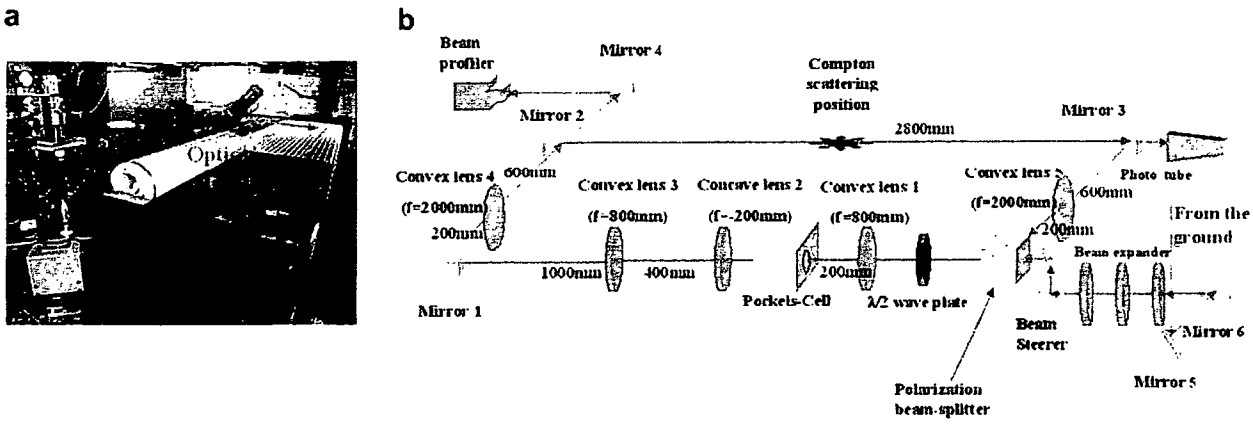

Fig. 3. Schematic layout of the high power laser pulse circulation system. Updated photograph of the laser pulse circulation system (a). We measure the laser position and beam size at the collision point by the beam profiler, and measure the laser intensity by the photo-multiplier (b).

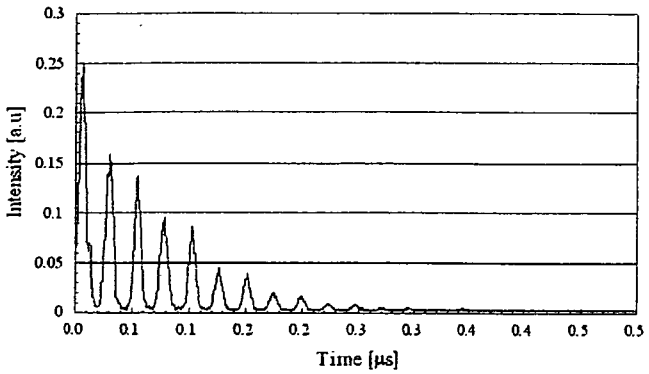

Fig. 4. Result of the laser circulation at 10 ns, 1.4 mJ, 532 nm (2nd harmonic) in the high power laser system.

We will carry out more precise alignment of optics system, and elucidate the polarization condition, the delay of the pockels-cell. Then, we are going to enhance the integrated laser energy and consequently the X-ray yield.

6. Conclusion

We are developing the compact monochromatic tunable X-ray source based on laser-electron Compton scattering. We have carried out the circulation experiment with the high power laser pulse circulation system. The laser pulse is circulated in the optical circuit more than 15 times, and the laser intensity is increased about 3.5 times at 10 ns, 1.4 mJ, 532 nm (2nd harmonic) in the first step. We will do further studies and experiments to elucidate the guideline of laser profiles control in future experiments. We will install optical devices that correspond to high power laser, and carry out laser pulse circulation experiments with the full power laser (1.4 J) this September. From October, we will carry out laser-electron Compton scattering experiments with the laser circulation system. We expect the X-ray intensity will increase up to 10^9 photons/s.

Acknowledgement

Part of this study is supported by Research Program on Development of Innovative Technology of Japan Science and Technology Agency.

References

[1] M. Torikoshi et al., IEEE Trans. Nucl. Sci. 50 (5) (2003).
[2] Katsuhiro Dobashi et al., Jpn. J. Appl. Phys. 44 (4A) (2005) 1995.
[3] Futaro Ebina et al., Nucl. Instr. and Meth. B 241 (2005) 905.
[4] Haruyuki Ogino et al., J. Nucl. Sci. Technol., in press.
[5] Tarek Mohamed et al., Optics Communications 214 (2002) 291.

Japanese Journal of Applied Physics
Vol. 45, No. 6A, 2006, pp. 5254–5262

Phase Tomography by X-ray Talbot Interferometry for Biological Imaging

Atsushi MOMOSE*, Wataru YASHIRO, Yoshihiro TAKEDA[1], Yoshio SUZUKI[2] and Tadashi HATTORI[3]

Department of Advanced Materials Science, School of Frontier Sciences, The University of Tokyo, 5-1-5 Kashiwanoha, Kashiwa, Chiba 277-8561, Japan
[1]*Graduate School of Pure and Applied Sciences, University of Tsukuba, 1-1-1 Tennodai, Tsukuba, Ibaraki 305-8573, Japan*
[2]*Japan Synchrotron Radiation Research Institute, 1-1-1 Kouto, Sayo, Hyogo 679-5198, Japan*
[3]*Laboratory of Advanced Science and Technology for Industry, University of Hyogo, 3-1-2 Kouto, Kamigori, Hyogo 678-1205, Japan*

(Received December 13, 2005; accepted March 5, 2006; published online June 8, 2006)

The X-ray phase tomography of biological samples is reported, which is based on X-ray Talbot interferometry. Its imaging principle is described in detail, and imaging results obtained for a cancerous rabbit liver and a mouse tail with synchrotron radiation are presented. Because an amplitude grating is needed to construct an X-ray Talbot interferometer, a high-aspect-ratio grating pattern was fabricated by X-ray lithography and gold electroplating. X-ray Talbot interferometry has an advantage that it functions with polychromatic cone-beam X-rays. Finally, the compatibility with a compact X-ray source is discussed. [DOI: 10.1143/JJAP.45.5254]

KEYWORDS: phase contrast, tomography, interferometry, Talbot effect, grating, cone beam

1. Introduction

The high sensitivity achieved by X-ray phase imaging methods has been attracting increasing attention.[1,2] Because conventional X-ray imaging methods rely on absorption in an object to be inspected, weak absorbing structures, such as biological soft tissues, cannot be imaged with a sufficient signal-to-noise ratio under the allowable X-ray dosage limit. The use of X-ray phase contrast provides a way to overcome this difficulty. This is because the interaction cross section of X-ray phase shift is about a thousand times larger than that of absorption for soft tissues.[3]

Several methods have been developed for X-ray phase imaging to date, which are categorized into the interferometric method,[4–7] refraction-based method,[8–11] and propagation-based method.[12–14] Besides the methods that only generate phase contrasts, phase measurement methods are also developed, enabling quantitative image analyses, such as phase tomography.[6,7,15–19]

X-ray phase imaging is very attractive from a clinical point of view because the sensitivity to soft tissues is tremendously increased and/or X-ray dose is considerably reduced, as compared with the conventional X-ray imaging methods. Nevertheless, the introduction of these methods to medical diagnosis is very slow. This is because X-ray sources with a quality much higher than that of conventional laboratory (or hospital) X-ray sources are required in most X-ray phase imaging methods.

As for methods using a crystal interferometer[4–7] or analyzer crystal for selecting refracted X-rays,[8–11,16–19] a restriction emerges from the fact that crystal optical elements are used. The crystal optics functions under the Bragg diffraction condition; therefore, a monochromatic and parallel beam is needed with a sufficient flux. As a result, synchrotron radiation is a sole choice available for those methods with practical imaging exposure time.

The propagation-based method[12–15] relies on the detection of Fresnel diffraction, by which an outline contrast is generated at the surface and structural boundaries of a sample. The width of the outline contrast is approximately $\sqrt{\lambda \ell}$, where λ and ℓ are the X-ray wavelength and distance between the sample and detecting plane, respectively. To resolve the outline contrast, whose width is of the order of microns even when an image is detected 1 m downstream from the sample, an image detector with an effective pixel size of the order of microns or smaller is needed. Because X-rays enough to ensure a sufficient signal-to-noise ratio are needed in a pixel, a brilliant X-ray source is required consequently. Many experiments are therefore performed at synchrotron facilities. The contribution of the outline contrast can be observed using a detector of a pixel size larger than the above estimation, and a medical apparatus has been developed on the basis of this usage for use in hospitals.[20] However, for quantitative phase measurement and thereby phase tomography, Fresnel diffraction must be observed with a sufficient spatial resolution and a sufficient signal-to-noise ratio, which are attained by synchrotron radiation.[15]

Recently, X-ray differential interferometry that employs transmission gratings has been studied for X-ray phase imaging,[21–25] which is potentially compatible with compact X-ray sources. X-ray Talbot interferometry (XTI)[22] shown in Fig. 1 is an X-ray differential interferometer consisting of a phase grating (G1) and an amplitude grating (G2). XTI may provide an opportunity for the instrumentation outside synchrotron facilities, because it functions in principle with a cone beam with a broad energy band width.

The principle of XTI is the same as that of optical Talbot interferometry,[26,27] but the fabrication of an amplitude

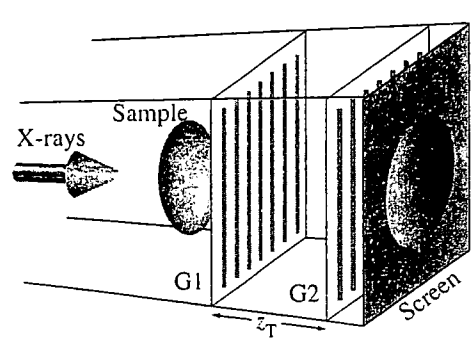

Fig. 1. Configuration of XTI, where two transmission gratings (G1 and G2) are arranged in line along X-ray axis.

*E-mail address: momose@exp.t.u-tokyo.ac.jp

X-ray grating is a difficulty that needs to be overcome to realize XTI. Because of the high penetrating power of X-rays, a thick pattern must be fabricated to block X-rays fully. At the same time, the period of the grating should be of the order of microns, as explained later according to the principle of XTI. The fabrication of a pattern with such a high aspect ratio is not straightforward.

A capillary plate, which has a two-dimensional array of holes in a lead glass plate with an aspect ratio that meets already the requirement for XTI, is a candidate device for the amplitude X-ray grating.[28] However, its quality, such as the uniformity of the pitch of the hole array, is currently unsatisfactory. A line and space (L&S) pattern is used for a simple and typical grating and available for XTI. However, the fabrication of a high-aspect-ratio L&S pattern is difficult using conventional lithographic techniques. However, X-ray lithography is attractive for that purpose, and in this study we used a grating fabricated by X-ray lithography and electroplating of gold,[29] which was selected as a material for blocking X-rays because of its high absorption coefficient and technical convenience in the fabrication process.

In this paper, theoretical aspects of XTI are described first, including the procedure of phase tomography. Then, we report evaluation results of an X-ray Talbot interferometer constructed with gold gratings. We performed phase tomography measurements on biological soft tissues with the interferometer using synchrotron radiation, and reconstructed images are presented next. Finally, future prospects of XTI are discussed.

2. X-ray Talbot Interferometry

2.1 Principle of phase imaging

The principle of XTI was described in a previous paper[22] but again described here, adding more details, for the following explanation of phase tomography based on XTI.

The function of XTI is based on the X-ray (fractional) Talbot effect[30] discovered originally in the visible light region,[31] which is known as a self-imaging effect by an object with a periodic structure under coherent illumination. While a transmission image becomes blurry with increasing distance from an object to an imaging plane under normal illumination, self-images are reconstructed at specific distances from a periodic object to an imaging plane by the Talbot effect. This phenomenon is understood as a result of Fresnel or Fraunhofer diffraction.

Let us consider a situation in which a grating of a period d is illuminated coherently with unit-amplitude plane-wave X-rays of wavelength λ. Given the complex transmission function $T(x, y)$ of the grating with a Fourier expansion series

$$T(x,y) = \sum_n \alpha_n \exp\left(2\pi i \frac{nx}{d}\right), \tag{1}$$

the wave field $E(x, y, z)$ behind the grating is written as

$$E(x,y,z) = \sum_n \beta_n(z) \exp\left(2\pi i \frac{nx}{d}\right) \tag{2}$$

under a paraxial approximation, where

$$\beta_n(z) \equiv \alpha_n \exp(-\pi i \lambda z n^2/d^2). \tag{3}$$

Here, the optical axis is parallel to the z axis, and the grating is on the (x, y) plane ($z = 0$) and has periodicity in the x direction. Equations (2) and (3) imply that the periodic pattern in the wave field varies and oscillates as induced by propagation. The intensity of the wave field is given by

$$I_s(x,y,z) = |E(x,y,z)|^2 = \sum_n a_n(z) \exp\left(2\pi i \frac{nx}{d}\right), \tag{4}$$

where

$$a_n(z) \equiv \sum_{n'} \beta_{n+n'} \beta^*_{n'}. \tag{5}$$

The distances z_T given by

$$z_T = md^2/\lambda, \tag{6}$$

where m is an integer for an amplitude grating or a half integer for a phase grating, are particularly interesting. If m is an even integer, $\beta_n(z_T) = \alpha_n$; therefore, a wave field whose complex amplitude is the same as the complex transmission function of the grating is generated (Talbot effect). If m is an odd integer, $\beta_n(z_T) = -\alpha_n$, and a wave field with a complex amplitude of $T(x + d/2)$ is generated (a case of fractional Talbot effect); that is, the contrast is inverted. When a phase grating is used, no intensity patterns are observed at the distances. However, if m is a half integer, the phase modulation pattern $T(x) = \exp[i\phi(x)]$ is converted into intensity patterns, which are also called self-images in this work, as given by

$$|E(x,y,z_T)|^2 = 1 \pm \sin\{\phi(x) - \phi(x + d/2)\}, \tag{7}$$

where $\pm$ corresponds to cases in which $m - 1/2$ is even and odd.[32] Visibility is therefore at the maximum when the magnitude of phase modulation is $\pi/2$ while a π phase grating is used in many applications because $\pm$1st-order diffractions are enhanced, suppressing the 0th order. The self-image of a $\pi/2$ phase grating is understood as a constructive superposition of interference fringes mainly between neighboring orders (i.e., 0th and $\pm$1st orders, $\pm$1st and $\pm$2nd orders, ...).

Under partial coherent illumination, the visibility of a self-image is degraded and its influence can be reflected in eq. (4) by replacing $a_n(z)$ with $\mu(n\lambda z/d)a_n(z)$, where μ is the complex degree of coherence, which is given by the Fourier transform of the distribution of an X-ray source, according to the van Cittert–Zernike theorem.[33]

Next, let us consider a case in which the incident X-ray wave is deformed due to the phase shift $\Phi(x, y)$ caused by an object placed in front of the grating. In this case, the self-image is also deformed as illustrated in Fig. 2 and its intensity is given by

$$I_s(x,y,z) = \sum_n a'_n(x,y,z) \exp\left[2\pi i \frac{n}{d}(x - z\varphi_x(x,y))\right], \tag{8}$$

where

$$\varphi_x(x,y) = \frac{\lambda}{2\pi} \frac{\partial \Phi(x,y)}{\partial x} \tag{9}$$

and $a_n(z)$ has been replaced with $a'_n(x, y, z)$, which takes into consideration the effect of X-ray attenuation by the sample. The amount of deformation is proportional to z.

It is therefore possible to detect the object by analyzing the deformed self-image by using an image detector with

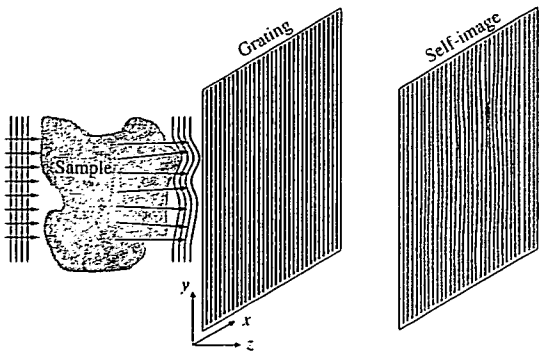

Fig. 2. Deformation of self-image by refraction at sample placed in front of grating.

a spatial resolution below d (of the order of microns). However, an X-ray image detector with such a resolution is rare. Instead XTI uses another grating at the position of the self-image, as illustrated in Fig. 1. If the period of the second grating is almost the same as that of the self-image, a moiré fringe pattern is generated by the superposition of the deformed self-image and the pattern of the second grating. The deformation of the self-image is also reflected on the moiré pattern. Because a typical fringe spacing is much larger than d, normal X-ray image detectors are available.

Giving the transmission function $t(x, y)$ of the second grating with a Fourier expansion series as

$$t(x, y) = \sum_n b_n \exp\left(2\pi i \frac{nx}{d}\right), \tag{10}$$

a moiré pattern is given by

$$I(x, y, z) = I_s(x, y, z) \times t(x, y)$$
$$= \sum_n a'_n(x, y, z) b_{\bar{n}} \exp\left\{2\pi i \frac{n}{d}(y\theta + z\varphi_x(x, y) + \chi)\right\}, \tag{11}$$

where θ ($\ll 1$) and χ are the relative inclination and displacement, respectively, in the (x, y) plane of the second grating against the first. The factor describing the contrast with the period of d has been averaged out.

2.2 *Phase tomography*

The X-ray phase shift $\Phi(x, y)$ is written as

$$\Phi(x, y) = \frac{2\pi}{\lambda} \int \delta(x, y, z)\, dz, \tag{12}$$

where $\delta(x, y, z)$ is the refractive index decrement from unity. Therefore, if phase shifts are measured in plural projection directions, $\delta(x, y, z)$ is reconstructed with the algorithm of computed tomography. This is X-ray phase tomography.[6] The quantitative measurement of $\Phi(x, y)$ is therefore significant. In the case of XTI, φ_x is determined from moiré patterns. Then, Φ is obtained by integration, enabling X-ray phase tomography.

To determine φ_x from the moiré patterns, phase-shifting interferometry (or fringe-scanning method)[34] is available. Normal phase-shifting interferometry assumes a two-beam interference, which generates a sinusoidal fringe profile in general given by $A + B\cos\Phi$, where A and B are the average intensity and fringe contrast. By introducing a phase difference that varies with a step of $2\pi/M$ (M: integer), interference patterns

$$I^{(k)}(x, y) = A(x, y) + B(x, y)\cos\left\{\Phi(x, y) + \frac{2\pi k}{M}\right\} \quad (k = 1, 2, \ldots, M) \tag{13}$$

are measured, and Φ is calculated using

$$\Phi(x, y) = \arg\left[\sum_{k=1}^{M} I^{(k)}(x, y) \exp\left(-2\pi i \frac{k}{M}\right)\right]. \tag{14}$$

In the case of XTI that causes multibeam differential interference, by changing χ in eq. (11) with a step of d/M (M: integer), moiré patterns

$$I^{(k)}(x, y, z_T) = \sum_n a'_n(x, y, z_T) b_{\bar{n}} \times \exp\left\{2\pi i \frac{n}{d}\left(y\theta + z_T\varphi_x(x, y) + \frac{kd}{M}\right)\right\} \tag{15}$$

are measured. If the 0th and ±1st orders are dominant, it is clear that the operation of eq. (14) is available; that is,

$$\frac{2\pi}{d}(y\theta + z_T\varphi_x(x, y)) = \arg\left[\sum_{k=1}^{M} I^{(k)}(x, y, z_T) \exp\left(-2\pi i \frac{k}{M}\right)\right]. \tag{16}$$

The influence of higher orders is considered as below. The substitution of eq. (15) into the right hand side of eq. (16) yields

$$\arg\left[\sum_n a'_n(x, y, z_T) b_{\bar{n}} C_{n,M} \times \exp\left\{i2\pi \frac{n}{d}(y\theta + z_T\varphi_x(x, y))\right\}\right], \tag{17}$$

where

$$C_{n,M} \equiv \sum_{k=1}^{M} \exp\left\{2\pi i \frac{k}{M}(n-1)\right\} = \begin{cases} M & \text{if } n - 1 = qM \\ 0 & \text{otherwise} \end{cases} \quad q\text{: integer.} \tag{18}$$

The combinations of n and M that yield non-zero values of $C_{n,M}$ are shown in Table I, which suggests that if a sufficiently large number is selected for M, the influence of higher orders is cancelled out and eq. (16) is available.[35]

Here, it should be noted that even orders can be ignored if the gratings have 1:1 L&S patterns. Then, when $M = 5$, the lowest order is ninth, which causes an error in calculating φ_x using eq. (16). The magnitude of such a high order is very small normally. In addition, actual grating patterns are not

Table I. Combinations of n and M indicated by "e" yield non-zero values of $C_{n,M}$ and cause errors in calculating φ_x using eq. (16).

M	Harmonics ($\lvert n\rvert$)							
	2	3	4	5	6	7	8	9
3	e	—	e	e	—	e	e	—
4	—	e	—	e	—	e	—	e
5	—	—	e	—	e	—	—	e
6	—	—	—	e	—	e	—	—
7	—	—	—	—	e	—	e	—
8	—	—	—	—	—	e	—	e

completely rectangular and the spatial coherency of X-rays that impinge on the gratings is normally incomplete. These factors decrease higher orders and contribute to reducing errors in calculating φ_x using eq. (16). Thus, $M = 5$ is a kind of magic number suitable for applying the technique of phase-shifting interferometry to XTI. The absorption contrast caused by the sample, which is involved in a'_n, is eliminated by this procedure, and the resultant image maps purely the differential phase shift φ_x.

Normally, φ_x is determined by measurements with and without a sample. Then, the effect of θ on eq. (16) is removed by subtraction. In addition, the effect of the imperfection of gratings and/or deformed wavefronts of incident X-rays are excluded as well.

The right term of eq. (16) involves the operation of arctangent, whose value ranges from $-\pi$ to π. Therefore, when X-rays are refracted partially exceeding the amount corresponding to the range, jumps between $-\pi$ and π are found in the resultant image obtained by the calculation of eq. (16). In such a case, we need a process for *unwrapping* the jumps by adding (subtracting) 2π to (from) one of the pixels neighboring across the jumps. When the jump lines are clear, the procedure is completed without errors. However, the jump lines become unclear occasionally when the data is noisy or when regions of steep value changes are contained. Sophisticated techniques are developed to enable unwrapping in such cases, and we used a cut-line algorithm[36] in the present study.

Finally, Φ is obtained by calculating

$$\Phi(x, y) = \frac{2\pi}{\lambda} \int \varphi_x(x, y)\, dx + C, \tag{19}$$

and the constant of integration C is determined by the fact that a sample is surrounded by a null region in the measurement by tomography; that is, $C = 0$. By repeating this measurement at various angular positions of the sample rotation, one can reconstruct $\delta(x, y, z)$ using a conventional algorithm in computed tomography.

One can skip this integration process if an algorithm with a filter function for beam-deflection optical tomography[37] is used; in the case of the convolution-backprojection method,

$$H(h\Delta x) = \begin{cases} \dfrac{1}{\pi^2 h \Delta x} & h\text{: odd} \\ 0 & h\text{: even} \end{cases} \tag{20}$$

is the filter function to be used, where Δx is the pixel size.

As a summary of this section, images at each image processing step described above are shown in Fig. 3 using the data of the phantom experiment reported previously.[23]

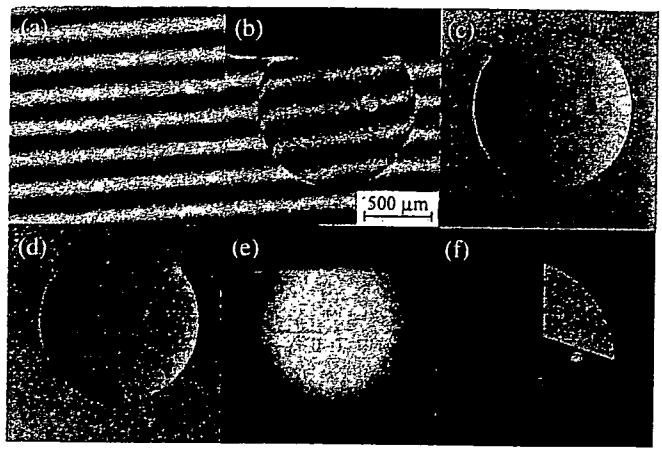

Fig. 3. Images at each step of phase tomography with XTI. A moiré pattern (a), which was due to the relative inclination (θ) of the grating against the other, is deformed by the differential phase shift caused by a sample (plastic sphere about 1 mm in diameter with some air bubbles in it) placed in the field of view, as shown in (b). (c) was obtained by a five-step fringe scan. The effect of θ was removed using (a). Because (c) is the output of eq. (16), the image is *wrapped*, and after an unwrapping procedure, (d) that exhibits φ_x is obtained. Black-white jumps observed in the outline region of the sphere in (c) are compensated. (e), which is to be input to the reconstruction algorithm of tomography, is obtained through the spatial integration of (d). Repeating this series of procedure at every angular position of the sample rotation, a three-dimensional image (f) mapping the refractive index is reconstructed, where one quadrant has been cropped to show the inside.

3. Experiments

3.1 Grating

We selected gold as a material for the grating pattern because its absorption coefficient is comparatively large. Nevertheless, the thickness should be much more than ten microns. As for the grating period, it should be smaller than or comparable to the X-ray spatial coherence length, which is several microns typically, and as a result a pattern of a high aspect ratio must be fabricated.

Although microfabrication by optical lithography is routinely performed, it is difficult to form a L&S pattern whose thickness exceeds ten microns. A solution is found in the field of X-ray lithography, which enables the formation of a high-aspect-ratio structure, taking advantage of the property of X-rays, that is, they tend to go straight in comparison with light of longer wavelengths. In this study, we used an X-ray amplitude grating fabricated by X-ray lithography and gold electroplating, as described below.

The synchrotron radiation beamline 11 of NewSUBARU, Japan, which is dedicated to Lithographie Galvanoformung Abformung (LIGA) fabrication, was used. A 30 μm X-ray resist film (MAX001, Nagase ChemteX) was spin-coated on a 200-μm Si wafer with a 0.25-μm Ti layer, and then a 4-μm L&S resist pattern ($d = 8\,\mu$m) was fabricated by X-ray exposure. Gold lines were formed by electroplating between resist lines, which were left after the electroplating to support the gold lines (Fig. 4). The effect of absorption by the X-ray resist is negligible. The height of the gold lines

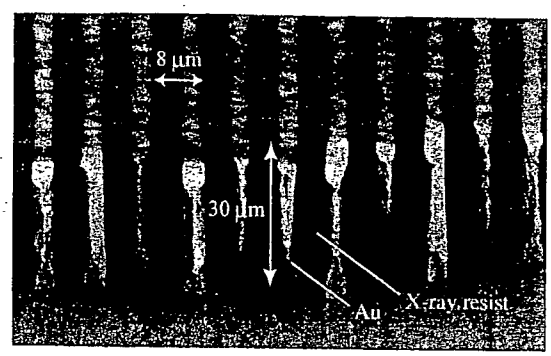

Fig. 4. SEM image of X-ray amplitude grating fabricated by X-ray lithography and gold electroplating. This grating was used for the second grating in XTI.

was nearly 30 μm, and the effective area of the grating was $20 \times 20\,mm^2$.[29]

The first grating was also fabricated in a similar manner, except that UV lithography was used, and had a gold pattern, which was much thinner than that of the second. The thickness was experimentally evaluated to be optimal for X-rays of about 0.065 nm for a $\pi/2$ phase grating. An amplitude grating is available for the first grating, but a phase grating is superior to an amplitude grating in that X-ray intensity is twice at an image detector and that the requirement for spatial coherency is moderated because z_T is reduced by one-half.

3.2 *Performance of XTI*

An X-ray Talbot interferometer was arranged at the beamline 20XU of SPring-8, Japan, where undulator X-rays were available at 245 m from the source point. The vertical source size of synchrotron radiation is normally much smaller than the horizontal size. However, because the effect of the instability of the beamline monochromator existed, the gratings were aligned so that the gold pattern was almost vertical. Then, spatial coherency was determined by horizontal source size. Strictly, in the present case, source size was determined by the front-end slit 400 μm in width located 214 m upstream from the grating. The spatial coherence was certainly larger than d (= 8 μm).

Figure 5 shows moiré patterns observed with 0.065-nm X-rays with the visibility as a function of the distance between the gratings. Here, θ was 1.3° and therefore the moiré fringes were generated. Although this study was performed assuming that synchrotron radiation is a plane wave, strictly a spherical wave with a small curvature was introduced into the interferometer, and its effect was observed as the inclination of fringes; that is, the horizontal component of spatial frequency is due to the mismatch of the period between the second grating and the self-image of the first grating, which was enlarged by slightly spherical-wave illumination.

At $z = d^2/2\lambda$, which was the best position for XTI with a $\pi/2$ phase grating, the fringe visibility exceeded 0.8. With increasing the distance, visibility minimized at $z \approx d^2/\lambda$ and again increased, indicating that this phenomenon was induced by the fractional Talbot effect. Strictly, a minimum was found at a distance slightly shorter than d^2/λ. This is considered to be due to the coexisting amplitude modulation caused by the first grating.

The influence of higher orders when using eq. (16) was commented above. Figure 6 shows the Fourier-transforms of the moiré patterns shown in Fig. 5. In Fig. 6(b), that is, the

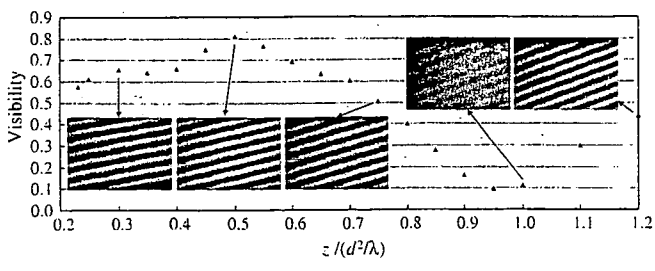

Fig. 5. Moiré patterns and their visibilities observed by XTI at various spacings between two gratings. $\lambda = 0.065$ nm.

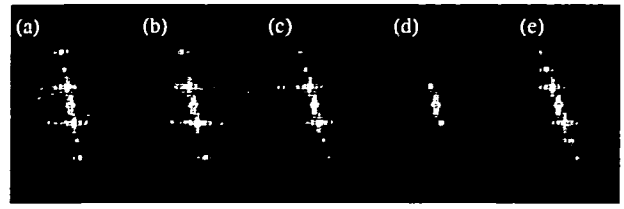

Fig. 6. Fourier-transforms of moiré patterns shown in Fig. 5 in the same order.

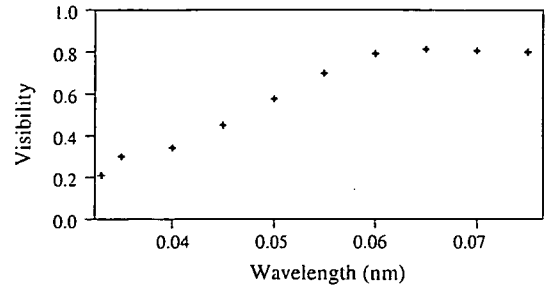

Fig. 7. Visibility of moiré pattern as function of X-ray wavelength. The distance between gratings was kept at $d^2/2\lambda$.

Fourier transform of the moiré pattern of the best visibility, spots of 0th, 1st, and 3rd orders existed, and those of higher orders and even orders were not detected. This result confirmed that the selection of 5 for M as discussed above was reasonable for the experiments of phase tomography that will be presented below. However, at the same time, it was found that other Fourier-transforms exhibited even orders as shown in Fig. 6. Therefore, one should be careful when XTI is operated with the grating separation widely different from $d^2/2\lambda$ even if the visibility is still high.

Next, keeping the condition $z = d^2/2\lambda$, the visibility was plotted as a function of λ (Fig. 7). This result shows that the Talbot interferometer functioned in a wide energy range; the visibility was over 0.3 even at 0.04 nm (31 keV). The availability of the interferometer at higher energy is meaningful because the observation of high-density tissues such as bone and calcification becomes more feasible, revealing soft tissue structures in the same view.

3.3 *Phase tomography of biological samples*

The X-ray Talbot interferometer was used for the tomographic observation of biological soft tissues. A sample was fixed on the tip of a rotation rod and immersed in formalin filling a cell. Because of the problem of bubble generation in the cell due to intense X-ray irradiation, beam intensity was moderately reduced by undulator-gap detuning. The flux density at a sample was approximately 10^{11} photons $mm^{-2}\,s^{-1}$.

The measurement of $\varphi_x(x, y)$ by a five-step fringe scan was repeated at each angular position of the sample rotation with a step of 0.72° over 180°. Images were recorded using a CCD camera coupled with optical lens and a phosphor screen, whose effective pixel size was 4.34 μm. The tomograms presented below are therefore formed by voxels 4.34 μm on one side. Exposure times for recording a moiré pattern were 1.0, 0.2, and 0.25 s for Figs. 8, 9, and 10, respectively.

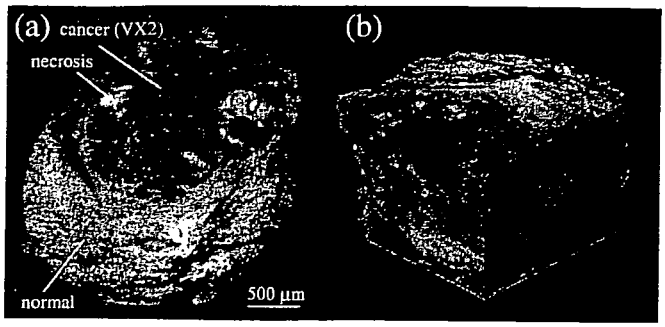

Fig. 8. Rabbit liver tissue with VX2 cancer examined by phase tomography with 0.1 nm X-rays. Cancerous lesion was clearly differentiated from normal tissue in (a), and necrosis in the tumor was revealed. (b) is a three-dimensional rendering view of a part of reconstructed data.

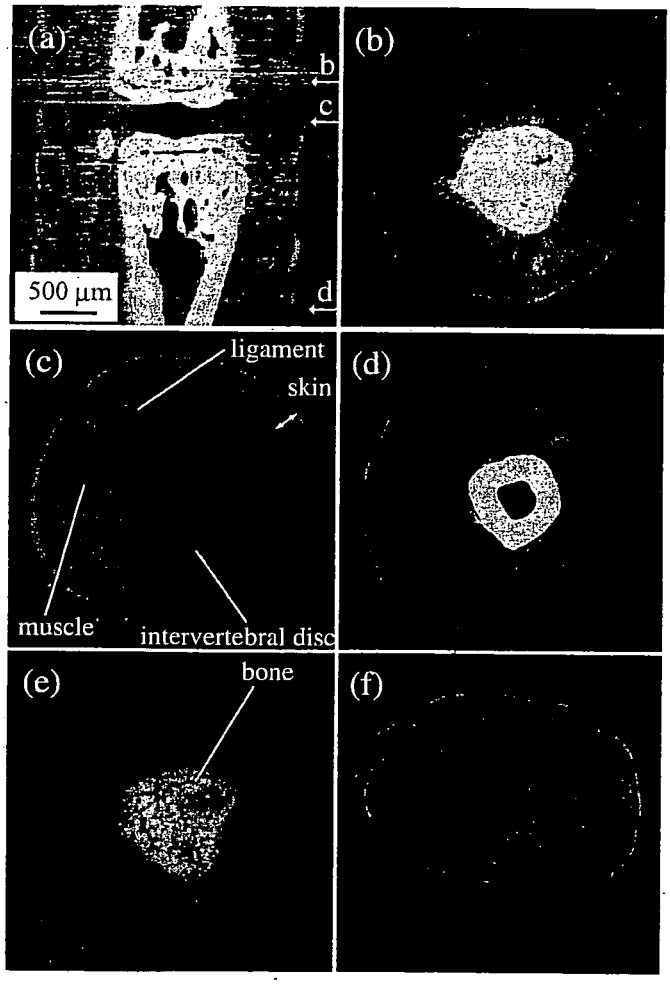

Fig. 9. Mouse tail observed by phase tomography with 0.07 nm X-rays. In the sagital image (a), the positions of the axial images (b), (c), and (d) are indicated by arrows. The grayscale of (b)–(d) corresponds to the refractive index difference ranging from 0 to 2×10^{-7}. A redrawing of (b) with a grayscale from 0 to 7×10^{-7} is shown in (e), where a trabecular structure of the bone is shown. (f) is a three-dimensional rendering view of a portion containing an intervertebral disc.

A piece of rabbit liver with cancer (VX2) was first examined using 0.1 nm X-rays. A cancerous lesion depicted with a lower grayscale value was clearly differentiated from a normal tissue as shown in Fig. 8. Furthermore, necrosis was detected as bright areas in the cancerous lesion. The grayscale corresponds to the refractive index difference ranging from 0 to 1.1×10^{-7}. This feature is comparable to the result obtained by phase tomography using a Mach–Zehnder type crystal X-ray interferometer.[38]

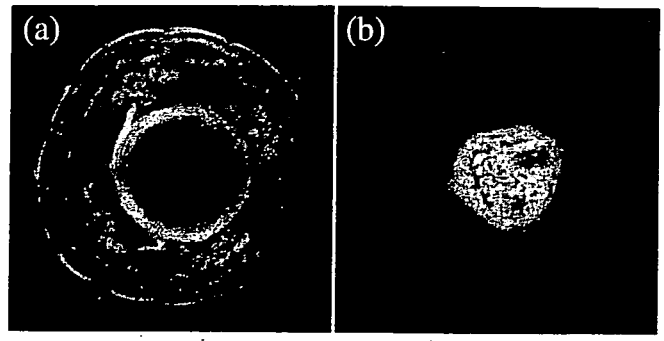

Fig. 10. Mouse tail identical to sample shown in Fig. 9, observed by phase tomography with 0.04 nm X-rays. The slice positions of (a) and (b) correspond to those of Figs. 9(c) and 9(e). The grayscales of (a) and (b) correspond to the refractive index difference ranging from 0 to 6×10^{-8} and to 2×10^{-7}, respectively.

XTI is available for a sample containing bone tissue, while phase tomography with a crystal X-ray interferometer is not suitable for such a sample because interference fringes that are too fine to resolve are generated by bones. Figure 9 shows a result obtained for a mouse tail using 0.07 nm X-rays. The arrows in the sagital image [Fig. 9(a)] indicate the positions of axial images shown in Figs. 9(b)–9(d). Soft tissue structures, such as muscle, ligament, skin, and intervertebral disc (cartilage), were depicted with bones in the same view although the bones generated some artifacts. The bones in these views are saturated, but a trabecular structure was depicted by changing the grayscale, as shown in Fig. 9(e).

It should be noted that the contrast of the bones does not include the contribution of absorption, which was eliminated by the operation in eq. (16). If the information of absorption is needed, it can be obtained by calculating amplitude instead of the argument as in the right term of eq. (16).

The X-ray Talbot interferometer functioned using 0.04 nm X-rays, as suggested by the result shown in Fig. 7. Therefore, the mouse tail was observed at this wavelength, as shown in Fig. 10, whose axial positions corresponded to those of Figs. 9(c) and 9(e). Although Fig. 10 seems to be slightly noisier than Fig. 9, one reason for which is the lower visibility of moiré fringes at 0.04 nm, this result fully suggests that our X-ray Talbot interferometer is available for X-ray phase tomography at this energy.

4. Discussion

4.1 Resolution

The spatial resolution of an image obtained by XTI is limited by the period of the grating. Including other factors such as the resolution of the image detector and noise, actual spatial resolution is determined. We evaluated spatial resolution on the basis of the average full width at half maximum (FWHM) of differential contrast profiles across boundaries between the sample and surrounding medium (formalin) in phase tomograms. From Figs. 8 and 10, 14 and 16 μm were obtained, respectively. To improve spatial resolution, gratings of a smaller period are necessary.

Contrast resolution, which describes the high sensitivity

of X-ray phase imaging, was evaluated on the basis of the standard deviation in the tomograms at the region of the surrounding formalin. In the X-ray energy region, the refractive index decrement δ, which phase tomography reveals as explained, is approximately given by

$$\delta = \frac{r_e \lambda^2}{2\pi} \rho, \tag{21}$$

where r_e is the classical electron radius and ρ is the electron density. This implies that the contrast in phase tomograms corresponds to a map of electron density. Furthermore, particularly for materials consisting of light elements, electron density is approximately proportional to mass density. Therefore, a phase tomogram is considered to be a mass density map. The standard deviation of voxel values in a part of the surrounding formalin region of Fig. 8 was 1.9×10^{-9}. The detection limit of density deviation was therefore estimated to be 1.3 mg/cm^3 because the δ of formalin, which is almost the same as that of water,[39] is 1.5×10^{-6} for 0.1 nm X-rays. Similarly, we obtained 2.2 and 5.9 mg/cm^3 for 0.07 and 0.04 nm X-rays, respectively, from Figs. 9 and 10. Thus, the sensitivity to density deviation is better with X-rays of longer wavelengths. This result is consistent with the fact that δ is proportional to the square of λ [eq. (21)].

However, it should be emphasized that errors in the unwrapping are reduced with decreasing wavelength. This is because a too strong refraction is suppressed moderately, therefore, a too rapid change in resultant φ_x is reduced. For samples containing high-density regions such as bone, the use of higher energy X-rays is significant in this sense.

4.2 *Requirements for X-ray beam quality*

The experiments reported in this paper were performed with synchrotron radiation assuming plane-wave monochromatic X-rays. However, as mentioned in the Introduction, XTI functions in principle with spherical-wave (cone-beam) X-rays with a broad energy band because of the use of grating optics. Here, the performance of XTI is discussed when polychromatic X-rays are used.

The change in φ_x caused by the spectral change $\Delta\lambda$ is given using eqs. (9), (12), and (21) by

$$\Delta\varphi_x = \Delta\lambda \frac{r_e \lambda}{\pi} \int \frac{\partial \rho}{\partial x} dz. \tag{22}$$

Because the positions of moiré fringes are determined by the maximum of $\cos(2\pi z_T \varphi_x / d)$, as suggested in eq. (11), the spectral change moves moiré fringes in proportion to

$$\frac{2\pi}{d} z_T \Delta\varphi_x = 2mr_e \Delta\lambda d \int \frac{\partial \rho}{\partial x} dz. \tag{23}$$

As a result, a finite band width causes a decrease in the visibility of moiré fringes. An acceptable band width so that moiré fringes are not smeared out is evaluated using

$$2mr_e \Delta\lambda\, d \int \frac{\partial \rho}{\partial x} dz < \frac{\pi}{2}. \tag{24}$$

Here, let us consider a case of detecting an air bubble in water. We assume that the pixel size of an image detector is d, which is the same as the period of the grating, since a smaller pixel size is meaningless because the spatial resolution of XTI is limited by d according to its principle. Then, the maximum gradient that would be measured with a discrete sampling is $\sqrt{D/d}$, where D is the diameter of the air bubble, and eq. (24) is rewritten as

$$4mr_e \Delta\lambda\, d\rho \sqrt{\frac{D}{d}} < \frac{\pi}{2}. \tag{25}$$

Using the parameters used in this study ($d = 8\,\mu$m, $m = 1/2$) and $\rho = 3.3 \times 10^{29}$ m^{-3} for water,

$$\Delta\lambda \sqrt{D} < 2.9 \times 10^{-13}, \tag{26}$$

where $\Delta\lambda$ and D are given with the unit of meter. This implies that $\Delta\lambda$ can be broaden up to 29 pm without smearing out an air bubble 100 μm in diameter in water. Thus, X-rays with a bandwidth $\Delta\lambda/\lambda \sim 0.1$ are certainly available. However, this result suggests at the same time that a narrower band should be selected so as to satisfy eq. (24) when a thicker object is observed.

The above discussion was presented neglecting the degradation of the performance of XTI by band width. Because z_T is inversely proportional to λ, the visibility of moiré fringes should be worse in the case of using polychromatic X-rays than in the case of using monochromatic X-rays. The contrast of the self-image has maxima along z every d^2/λ, as suggested by eq. (6). Assuming that the change in z_T induced by the spectral change of $\pm\Delta\lambda$ is smaller than $(1/4)(d^2/\bar{\lambda})$, a condition that moiré fringes are visible would be given by

$$\frac{\Delta\lambda}{\bar{\lambda}} < \frac{1}{8}, \tag{27}$$

where $\bar{\lambda}$ is the central wavelength. Thus, XTI is tolerant of the broadness of X-ray spectrum.

The above result implies that XTI does not require temporal coherency for its operation. However, requirement for spatial coherency should be noted. From the viewpoint of geometrical optics, the Talbot effect is understood as a result of interference mainly between neighboring diffraction orders generated by the grating. The angular difference between two beams of neighboring orders is λ/d, and therefore an interference fringe pattern, or self-image, with a period d is formed. Because the two beams are spatially separated by $\lambda z_T/d = md$ at $z = z_T$, the spatial coherence length should be approximately larger than md, in the case of presented study $d/2$.

In general, the spatial coherence length L is defined by

$$L = \frac{\lambda R}{2\pi\sigma_x}, \tag{28}$$

at the distance R from an X-ray source with a Gaussian intensity distribution $\exp(-x^2/2\sigma_x^2)$. Figure 11 shows the fringe visibilities of the self-image of a $\pi/2$ phase grating at $z = d^2/2\lambda$ as a function of L/d. The visibility curve is independent of λ, and when the coherence length is larger than one-half of the grating period, a self-image with a visibility of more than 0.7 is produced, which is enough for phase imaging provided the pattern of the second grating is sufficiently thick. It is noteworthy that a visibility of 0.4 is attained even $L/d \approx 1/3$.

4.3 *Prospects*

As presented, phase imaging at 0.04 nm was successful,

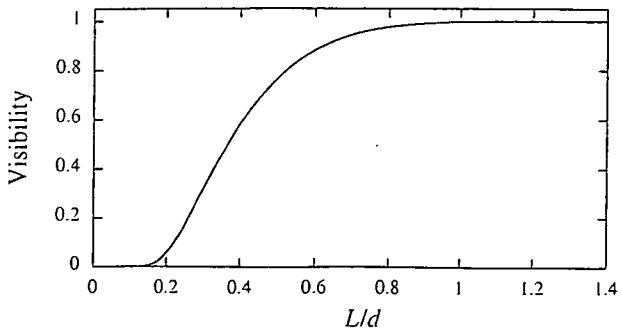

Fig. 11. Visibility of self-image of $\pi/2$ phase grating at $z = d^2/2\lambda$ as function of ratio of coherence length (L) and period of grating (d).

but it is of course necessary to fabricate a thicker pattern to attain a better imaging quality at this or a higher-energy region. At the same time, the area of the grating should be increased for practical imaging applications. The period of the gratings is also preferred to be shortened because the system can be compact and the requirement for spatial coherency is moderated. We consider that such developments are possible by improving the fabrication technology used in this study.

Although this study demonstrated XTI with synchrotron radiation, which can be assumed to be plane-wave X-rays, the development of cone-beam XTI with a compact X-ray source is significant for practical applications. The principle of XTI is common in cone-beam XTI, aside from some modifications. When a spherical wave is used, the positions of self-imaging given by eq. (6) for the plane-wave case must be replaced by

$$z_T = \frac{md_1^2 R}{R\lambda - md_1^2}, \tag{29}$$

where R is the distance between the source and the first grating with a period d_1.[40] The period d_2 of the second grating is different from d_1 and has a relation

$$d_1 : d_2 = R : (R + z_T). \tag{30}$$

Although the use of spherical gratings would be ideal in this case, flat gratings are also available for XTI with a spherical wave, provided that R is sufficiently larger than the size of the field of view, theoretical considerations on which will be described elsewhere.[41]

As for an image detector, XTI does not require a spatial resolution as high as that for resolving the self-image. Therefore, a variety of X-ray image detectors should be compatible with XTI. Here, it should be noted that an image detector in combination with the two gratings can be considered as a phase-sensitive image detector. In this sense, XTI is a breakthrough for the development of the first X-ray wavefront sensor.

Because XTI is operated with a cone beam with a broad energy band, its instrumentation outside synchrotron radiation facilities is highly expected. What types of X-ray source are available for cone-beam XTI? Normal X-ray generators used in hospitals are not available because of the lack of spatial coherency. The source size and source-grating distance must be selected to produce a spatial coherence length enough to generate the Talbot effect. It is therefore preferable to use a small source at a position far from it [see eq. (28)]. For instance, if $d_1 = 5\,\mu\text{m}$, $\lambda = 0.04\,\text{nm}$, and $\sigma_x = 5\,\mu\text{m}$ (FWHM of the source size is about $12\,\mu\text{m}$), then R should be larger than 2 m. At the same time, a sufficient flux is needed for imaging with a practical exposure time. These two requirements are contrary to each other.

Assuming that 10^3 photons/s are needed per $50\,\mu\text{m}$ pixel for phase imaging and that a field of view of $100 \times 100\,\text{mm}^2$ is covered with an array of pixels, an X-ray source emitting 2×10^{13} photons/s in the entire solid angle is required under the above conditions with respect to σ_x and R. Even taking into account the bandwidth available for XTI discussed above, the wattage of such an X-ray source should be over 100 W, which is much higher than that of commercially available microfocus X-ray generators. Although the requirement for X-ray sources is moderated using XTI as discussed above, we need to make an effort as well to develop a microfocus X-ray source with an improved brightness for practical phase imaging by XTI.

5. Conclusions

The principle of X-ray phase imaging and phase tomography with XTI was described, and successful biological imaging results with synchrotron radiation were presented. The key for the construction of an X-ray Talbot interferometer is the fabrication of an amplitude grating, because a high-aspect-ratio pattern must be formed. We fabricated a gold grating by X-ray lithography and electroplating. The X-ray Talbot interferometer with the gold grating functioned with synchrotron X-rays down to 0.04 nm wavelength. Provided that a grating with a higher aspect ratio and a wider effective area is fabricated, XTI is an attractive candidate for practical X-ray phase imaging, such as that for clinical diagnoses, because XTI has an advantage in that cone-beam X-rays of a broad energy band are available, allowing its compatibility with a compact X-ray source.

Acknowledgements

We appreciate the biological samples provided by Drs. J. Wu and T. Takeda (University of Tsukuba, Japan), the use of which was approved by the Medical Committee for the Use of Animals in Research of University of Tsukuba. The experiments using synchrotron radiation were performed under the approval of SPring-8 committee 2005A0326-NM-np. This study was financially supported by the project "Development of System and Technology for Advanced Measurement and Analysis" of Japan Science and Technology Agency (JST).

1) R. Fitzgerald: Phys. Today **53** (2000) 23.
2) A. Momose: Jpn. J. Appl. Phys. **44** (2005) 6355.
3) A. Momose and J. Fukuda: Med. Phys. **22** (1995) 375.
4) U. Bonse and M. Hart: Appl. Phys. Lett. **6** (1965) 155.
5) M. Ando and S. Hosoya: Proc. 6th Int. Conf. X-ray Optics and Microanalysis, Tokyo, 1972, p. 63.
6) A. Momose: Nucl. Instrum. Methods Phys. Res., Sect. A **352** (1995) 622.
7) F. Beckmann, U. Bonse, F. Busch and O. Günnewig: J. Comput. Assist. Tomogr. **21** (1997) 539.
8) V. A. Somenkov, A. K. Tkalich and S. Sh. Shil'shtein: Sov. Phys. Tech. Phys. **36** (1991) 1309.
9) T. J. Davis, D. Gao, T. E. Gureyev, A. W. Stevenson and S. W. Wilkins: Nature **373** (1995) 595.